



Structural evolution of robust Ni₃Fe₁ alloy on Al₂O₃ in dry reforming of methane: Effect of iron-surplus strategy from Ni₁Fe₁ to Ni₃Fe₁

Yubin Li ^{a,1}, Qianqian Wang ^{a,1}, Min Cao ^a, Sha Li ^{a,b,*}, Zhiwen Song ^a, Li Qiu ^a, Feng Yu ^a, Ruifeng Li ^{a,c}, Xiaoliang Yan ^{a,c,d,*}

^a College of Chemical Engineering and Technology, Taiyuan University of Technology, Taiyuan, Shanxi 030024, PR China

^b College of Textile Engineering, Taiyuan University of Technology, Taiyuan, Shanxi 030024, PR China

^c State Key Laboratory of Clean and Efficient Coal Utilization, Taiyuan University of Technology, Taiyuan, Shanxi 030024, PR China

^d Shanxi Key Laboratory of Compound Air Pollutants Identification and Control, Taiyuan University of Technology, Taiyuan, Shanxi 030024, PR China



ARTICLE INFO

Keywords:

Ni–Fe alloy
Dry reforming of methane
Stability
Dealloying process
Reaction mechanism

ABSTRACT

Bimetallic Ni–Fe alloy catalyst offers boosting effect for dry reforming of methane (DRM) by strong interaction between Ni and Fe. However, the facile segregation of iron species from the alloy particles remains an open challenge. Herein, in pursuit of a stable Ni–Fe alloy, Ni₁Fe₁/Al₂O₃ and Ni₃Fe₁/Al₂O₃ catalysts were developed by an evaporation-induced self-assembly method. Ni₁Fe₁/Al₂O₃ exhibited superior stability to Ni₃Fe₁/Al₂O₃ at 600 °C for 50 h. The structural evolution of Ni–Fe alloys existed on Ni₁Fe₁/Al₂O₃ and Ni₃Fe₁/Al₂O₃ in DRM, leading to the generation of Ni₃Fe₁/Al₂O₃ and Ni/Al₂O₃, respectively, where the equimolar alloy provided sufficient FeO_x in the dealloying process. Compared to Ni₃Fe₁/Al₂O₃, Ni₁Fe₁/Al₂O₃ possessed smaller amounts of coke deposition with lower graphitization, which is beneficial to realloying of the segregated FeO_x for Ni–Fe alloy. Furthermore, the two catalysts presented distinct pathways for coke deposition, where CO and CH₄ dissociation concurrently occurred on Ni₃Fe₁/Al₂O₃, while only CH₄ dissociation appeared on Ni₁Fe₁/Al₂O₃.

1. Introduction

Dry reforming of methane (DRM) has been well recognized as an environmentally and economically viable and dependable approach to effectively convert greenhouse gases (CH₄ and CO₂) to industrially valuable syngas (CO and H₂) (Eq. 1). Oxides supported Ni catalysts were found to be promising candidates with comparable activity as supported noble-metal catalysts [1–5]. However, the main origin for severe decline of catalytic performance on supported Ni catalysts can be traced to coke deposition (blocking the metal surface by the formation of carbon structures) from CH₄ and CO dissociation (Eqs. 2 and 3) [6–10].



From an economic and industrial point of view, bimetallic Ni–Fe

catalysts have been designed and developed to meet the desirable criteria with high resistance towards coke formation in DRM [11]. Considering the reaction mechanism of DRM, CH₄ is dissociated into CH_x* and H* on the surface of Ni regardless of bi-functional or mono-functional pathway, where active carbon atoms (*C) from subsequent CH_x dissociation on Ni are prone to accumulate and polymerize to coke [2,12–15]. By introducing a second metal, such as Fe to supported Ni catalysts, the active surface on Ni particles could be passivated by the formation of alloy structure, leading to a retarded carbon deposition rate from CH₄ dissociation [16,17]. Besides, being more oxyphilic than Ni, Fe has been proved to facilitate the conversion of carbon species (carbon gasification) by the presence of FeO_x towards CO₂ oxidation (Eqs. 4 and 5) [18,19].



The close and intimate interactions between Ni and Fe on Ni–Fe alloy are beneficial to enhance the coke resistance by the Mars–van

* Corresponding authors: College of Chemical Engineering and Technology, Taiyuan University of Technology, Taiyuan, Shanxi 030024, PR China.

E-mail addresses: lisha@tyut.edu.cn (S. Li), yanxiaoliang@tyut.edu.cn (X. Yan).

¹ Yubin Li and Qianqian Wang contributed equally to this work.

Krevelen (MvK) mechanism, where CH_4 and CO_2 activation occurs on Ni and Fe, respectively [17–24]. However, Ni–Fe alloy tends to be excessively oxidized as evidenced by the formation of Ni-rich alloy with separate phase of Ni and FeO_x in previous work [11,25]. This dealloying process on Ni–Fe alloy catalysts proceeds with the formation of superfluous FeO_x , which covers the Ni catalysts and is detrimental to catalytic performance in DRM. It has been reported that the oxidized Fe^{2+} species (FeO) partially migrated into the $\text{Mg}(\text{Al})\text{O}$ support or further formed highly stable LaFeO_3 solid solution on La_2O_3 , which encapsulated the dealloyed Ni particles and blocked the active Ni sites, being inaccessible to CH_4 activation [22,26].

Great endeavors have been made to stabilize the Ni–Fe alloy structures, for instance, by establishing realloying pathway and protection shell [20,27]. Specifically, Kim et al. proposed a $\text{Fe}^{2+}\text{O}/\text{Fe}^0$ redox cycle on Ni–Fe catalyst to establish a reversible realloying pathway from Ni– FeO to Ni–Fe alloy [20]. The oxidized Fe with a few atoms layer thickness was closely interacted with Ni sites on Ni– FeO (a fraction of FeO on Ni-rich particles), and the resultant FeO could react with carbon deposits on Ni sites, contributing to a reduced coke formation for 10 h test. Theofanidis et al. used a thin protection of surface layer containing Fe–Ni–Pd to reduce the segregation of Fe from the alloy particles [27]. Fe–Ni–Pd shell stabilized the Fe–Ni core and protected the core structure as a barrier for Fe segregation. An optimal composition of Ni to Pd ratio increased the activity and stability of Ni–Fe catalyst during DRM up to 21 h. However, tailoring the properties of the intimate interactions between Ni and counterpart Fe on widely-used Al_2O_3 without additional modification remains challenging in designing a robust alloy structure in long-term DRM.

It has been reported that Fe seems inactive for CH_4 activation, therefore, the mole ratio of Ni to Fe on Ni–Fe alloy should be optimized with the value higher than 1:1, where Ni-rich alloy is favor for activity in DRM [18,19]. However, it is concurrently inevitable for the segregation of Fe from the alloy with time on stream to some extent, which results to the declined catalytic performance by coke formation. Described herein, we present an iron-surplus strategy to produce stable Ni–Fe alloy by the structural evolution from Ni_1Fe_1 to Ni_3Fe_1 alloy during DRM. First, without any protective agent, Ni^{2+} - and Fe^{3+} -containing ethanol solution were homogeneously mixed with aluminum gel from the peptization of industrial ALOOH. The obtained mixture as the starting material was dried to form powder sample by a standard evaporation-induced self-assembly (EISA) approach. Without modification by other promoters, Al_2O_3 supported Ni–Fe alloy catalysts were generated, which exhibited large surface area ($200 \text{ m}^2 \text{ g}^{-1}$) with mesoporous structure (15–20 nm) and good thermal stability. Afterwards, the uniform Ni_1Fe_1 and Ni_3Fe_1 alloys over Al_2O_3 were used for DRM, and possessed distinct catalytic behaviors for the reaction at 600 °C with 50 h period of time on stream. Specifically, the catalytic performance of directly reduced Ni_3Fe_1 alloy decreased in the initial period and stabilized at low conversions of CH_4 and CO_2 , whereas the improved stability on the equimolar Ni_1Fe_1 alloy were observed, which underwent structural evolution to stable Ni_3Fe_1 alloy during DRM. On the basis of in situ characterizations, it is demonstrated that the resultant Ni_3Fe_1 alloy from structural evolution of iron-surplus induced Ni_1Fe_1 alloy rather than from direct reduction under H_2 could change coke deposition pathway, prohibit the carbon deposit rate, and decline the crystalline of carbon species during the dealloying process in DRM.

2. Experimental

2.1. Preparation of Ni–Fe alloy catalysts

Bimetallic catalysts, including Ni_3Fe_1 and Ni_1Fe_1 alloys on Al_2O_3 , were synthesized by an EISA approach, as reported in our previous work [25]. Aluminum gel in a translucent white color was produced from the peptization of ALOOH (2.4 g), which was treated by concentrated nitric acid (551.6 μL volume with 30 mL of distilled water) under microwave

irradiation at 70 °C for 1 h with a stirring rotation speed of 300 r min^{-1} . The obtained gel was then cooled down to room temperature after the microwave treatment. Then, P123 (5 g) was dissolved into 40 mL of ethanol, and nickel nitrate hexahydrate and iron nitrate nonahydrate were dissolved into the ethanol solution, where 0.8419 g of $\text{Ni}(\text{NO}_3)_2 \cdot 6 \text{ H}_2\text{O}$ and 0.4097 g of $\text{Fe}(\text{NO}_3)_3 \cdot 9 \text{ H}_2\text{O}$ were used for the formation of Ni:Fe mass ratio of 3:1 or 0.5612 g of $\text{Ni}(\text{NO}_3)_2 \cdot 6 \text{ H}_2\text{O}$ and 0.8193 g of $\text{Fe}(\text{NO}_3)_3 \cdot 9 \text{ H}_2\text{O}$ were used for the generation of Ni:Fe mass ratio of 1:1. Afterwards, the aluminum gel was mixed with metal-containing solution, and the obtained mixture was stirred at room temperature for 4 h, and was subsequently placed into a glass Petri dish. Next, the EISA process was conducted to evaporate the solvent by two step drying process first at 60 °C for 48 h, and then at 100 °C for 48 h until the presence of flake-like composite. The fresh $\text{Ni}_3\text{Fe}_1/\text{Al}_2\text{O}_3$ and $\text{Ni}_1\text{Fe}_1/\text{Al}_2\text{O}_3$ were generated by the calcination of the composites with a heating ramp of 1 °C min^{-1} from room temperature to 500 °C for 4 h under air. The loading content of metal Ni and Fe is 7.25% and 2.49% for $\text{Ni}_3\text{Fe}_1/\text{Al}_2\text{O}_3$, and 4.98% and 5.03% for $\text{Ni}_1\text{Fe}_1/\text{Al}_2\text{O}_3$, respectively, as determined by the inductively coupled plasma optical emission spectrometry (ICP–OES) analysis. Furthermore, the $\text{Ni}_3\text{Fe}_1/\text{Al}_2\text{O}_3$ and $\text{Ni}_1\text{Fe}_1/\text{Al}_2\text{O}_3$ alloy catalysts were produced under direct H_2 reduction of the corresponding fresh catalysts at 700 °C for 1 h.

2.2. Characterizations

ICP–OES, powder X-ray diffraction (XRD), transmission electron microscope, high angle annular dark-field-scanning transmission electron microscopy, energy dispersive spectroscopy, Raman spectroscopy, and temperature programmed oxidation measurement were used to characterize Ni–Fe alloy catalysts before and after reaction. In situ XRD, in situ X-ray photoelectron spectroscopy, in situ Fourier transform infrared, and temperature-programmed surface reaction were employed to monitor structure changes and reaction intermediates during DRM. Methods for the characterizations in details were shown in supporting information.

2.3. Catalytic performance

DRM was performed at atmospheric pressure in a quartz fixed-bed reactor (450 mm of length and 8 mm of diameter), in which 50 mg of catalysts (20–40 mesh) and 1 g of quartz sand (20–40 mesh) were packed between two layers of quartz wool. Before the stability test, the temperature of the catalysts was heated up to 700 °C under Ar (30 mL min^{-1}), and then the catalysts were reduced at the same temperature for 1 h under H_2 (30 mL min^{-1}). Next, the temperature was declined to 600 °C under Ar and the feed gases were switched into the reactor for 50 h. CH_4 (99.999%) and CO_2 (99.999%) with a mole ratio of 1:1 were introduced into the reactor, and the gas hour space velocity was maintained at 60,000 $\text{mL g}^{-1} \text{ h}^{-1}$. The emission of gases was monitored and analyzed by an online gas chromatograph (Agilent 7820 A, with a TDX-1 column of 1 m). CH_4 and CO_2 conversions (X_{CH_4} and X_{CO_2}) and H_2/CO ratio were calculated on the basis of following equations.

$$\text{CH}_4\text{ conversion : } X_{\text{CH}_4} = \frac{F_{\text{CH}_4,\text{in}} - F_{\text{CH}_4,\text{out}}}{F_{\text{CH}_4,\text{in}}} \times 100\% \quad (6)$$

$$\text{CO}_2\text{ conversion : } X_{\text{CO}_2} = \frac{F_{\text{CO}_2,\text{in}} - F_{\text{CO}_2,\text{out}}}{F_{\text{CO}_2,\text{in}}} \times 100\% \quad (7)$$

$$\text{H}_2 / \text{CO ratio : } \text{H}_2 / \text{CO} = \frac{F_{\text{H}_2}}{F_{\text{CO}}} \quad (8)$$

where $F_{i,\text{in}}$ and $F_{i,\text{out}}$ refer to the molar flow rate (mol s^{-1}) of CH_4 or CO_2 in the inlet and outlet flows, respectively.

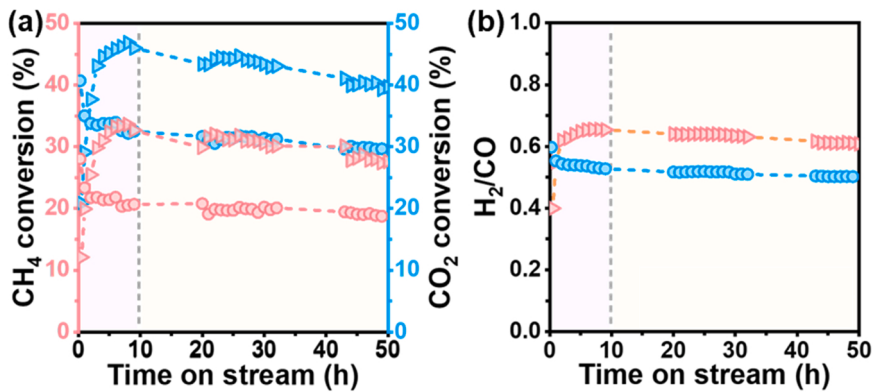


Fig. 1. (a) CH₄ conversion, CO₂ conversion and (b) H₂/CO ratio on Ni₃Fe₁/Al₂O₃ (circle) and Ni₁Fe₁/Al₂O₃ (triangle) catalysts for DRM at 600 °C for 50 h.

2.4. Kinetic study

Kinetic study of Ni₁Fe₁/Al₂O₃ was performed for the calculation of activation energy and reaction order, as shown in [Supporting information](#).

3. Results

3.1. Catalytic evaluation of Ni₃Fe₁/Al₂O₃ and Ni₁Fe₁/Al₂O₃ catalysts during DRM

CH₄ and CO₂ conversions as well as H₂/CO ratio on Ni₃Fe₁/Al₂O₃ and Ni₁Fe₁/Al₂O₃ catalysts as a function of reaction time at 600 °C are shown in Fig. 1a and b. CH₄ and CO₂ conversions on Ni₃Fe₁/Al₂O₃

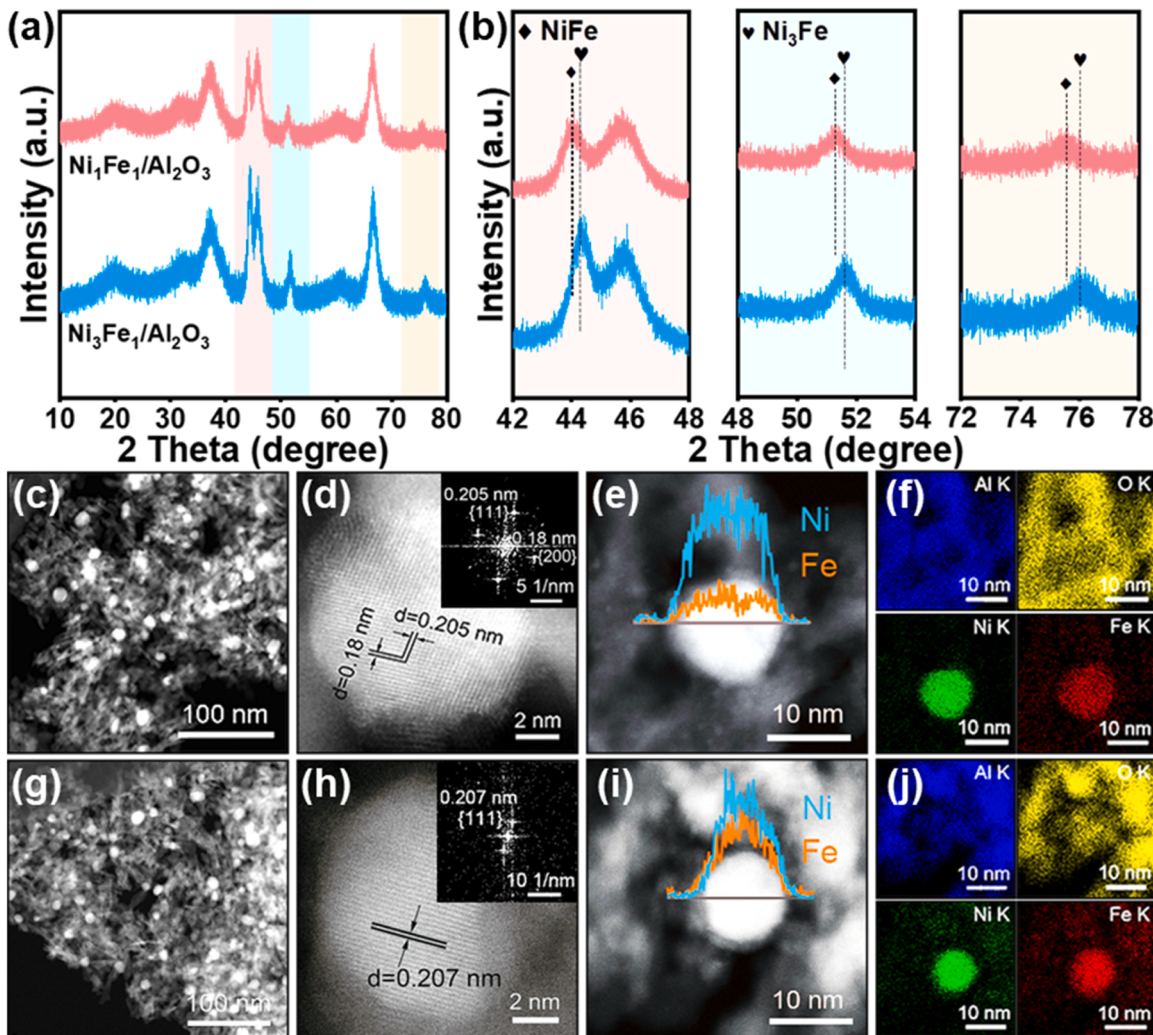


Fig. 2. (a, b) XRD patterns, (c, g) HAADF-STEM images, (d, h) HRTEM images and (e, i) EDS line scanning and (f, j) mappings of (c–f) Ni₃Fe₁/Al₂O₃ and (g–j) Ni₁Fe₁/Al₂O₃.

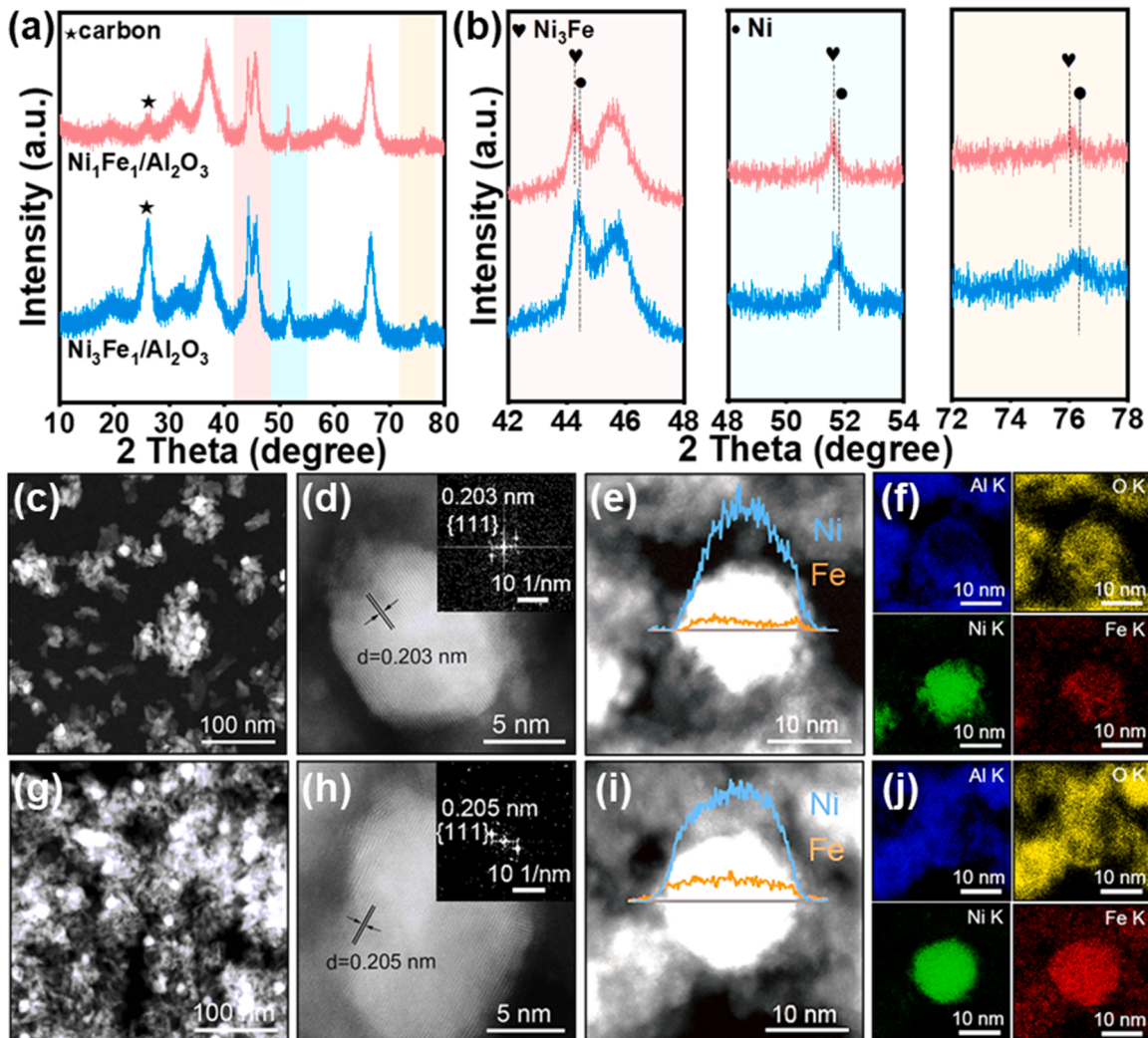


Fig. 3. (a, b) XRD patterns of the spent Ni₃Fe₁/Al₂O₃ and Ni₁Fe₁/Al₂O₃ catalysts after stability test. HAADF-STEM images, HRTEM images and EDS line scanning and mappings of the spent (c–f) Ni₃Fe₁/Al₂O₃ and (g–j) Ni₁Fe₁/Al₂O₃.

declined rapidly from 28% to 21% and from 41% to 32%, separately, in the first 2 h reaction during DRM (the pink and blue circles represent CH₄ and CO₂ conversions in Fig. 1a, respectively). The final CH₄ and CO₂ conversions on the catalyst dropped to 18% and 30%, respectively, with a slow decreasing rate after 10 h. Fig. 1b shows that H₂/CO ratio exhibited the similar trend with the conversions, which reduced from 0.6 to 0.54 in the first 2 h and maintains at 0.5 with time on stream. The results of catalytic deactivation on Ni₃Fe₁/Al₂O₃ were analogous to that of other Ni–Fe alloy catalysts during the stability study in the literature [17,27–29]. However, Ni₁Fe₁/Al₂O₃ exhibited distinct catalytic behavior in comparison with that of Ni₃Fe₁/Al₂O₃. The initial CH₄ and CO₂ conversions on Ni₁Fe₁/Al₂O₃ were 12% and 20%, which increase up to 34% and 47% in the first 10 h reaction, respectively (the pink and blue triangles refer to CH₄ and CO₂ conversions in Fig. 1a, respectively). Slightly decline of the conversions were observed with extending the reaction time, and the final CH₄ and CO₂ conversions on the catalyst reached to 28% and 40%, respectively. H₂/CO ratio on Ni₁Fe₁/Al₂O₃ increased from 0.4 to 0.65 in the first 10 h and stabilized at 0.6 during DRM. The equilibrium CH₄ and CO₂ conversions, as well as H₂/CO ratio are 41%, 54% and 0.73 at 600 °C (Fig. S1). It can be seen that CH₄ and CO₂ conversions as well as H₂/CO ratio on Ni₁Fe₁/Al₂O₃ were within the range of the thermodynamic equilibrium.

It should be noted that CH₄ and CO₂ conversions along with H₂/CO ratio on Ni₁Fe₁/Al₂O₃ after 50 h period reaction approached to the

initial values of those on Ni₃Fe₁/Al₂O₃. In order to deeply understand the beneficial effects of structural evolution from the equimolar Ni_{Fe}₁ alloy to Ni₃Fe₁ alloy during DRM, we further performed a series of characterizations, analyses and discussions in the following sections.

3.2. Characterizations of Ni–Fe alloy catalysts after reduction

The structures of the reduced Ni–Fe alloy on Ni₃Fe₁/Al₂O₃ and Ni₁Fe₁/Al₂O₃ before reaction were systematically investigated by X-ray diffraction (XRD) and high angle annular dark-field scanning transmission electron microscopy (HAADF-STEM) with energy dispersive spectroscopy (EDS) measurements (Fig. 2). Fig. 2a and b show that Ni–Fe alloy structures appeared on the XRD patterns of Ni₃Fe₁/Al₂O₃ and Ni₁Fe₁/Al₂O₃, besides the presence of the support (NiAl₂O₄ and Al₂O₃ reported in our previous work) [25]. For Ni₃Fe₁/Al₂O₃, the diffraction peaks at 44.3°, 51.5° and 75.9° corresponded to the (111), (200) and (220) planes of Ni₃Fe₁ alloy (PDF No. 38–0419). For Ni₁Fe₁/Al₂O₃, the peaks at 43.9°, 51.2° and 75.4° were attributed to the presence of (111), (200) and (220) planes of Ni₁Fe₁ alloy (PDF No. 12–0736).

The fine structures of Ni–Fe alloy on Ni₃Fe₁/Al₂O₃ and Ni₁Fe₁/Al₂O₃ were examined by using aberration-corrected HAADF-STEM. Representative STEM and high-resolution transmission electron microscopy (HRTEM) images are shown in Fig. 2c, d, g and h. The two catalysts

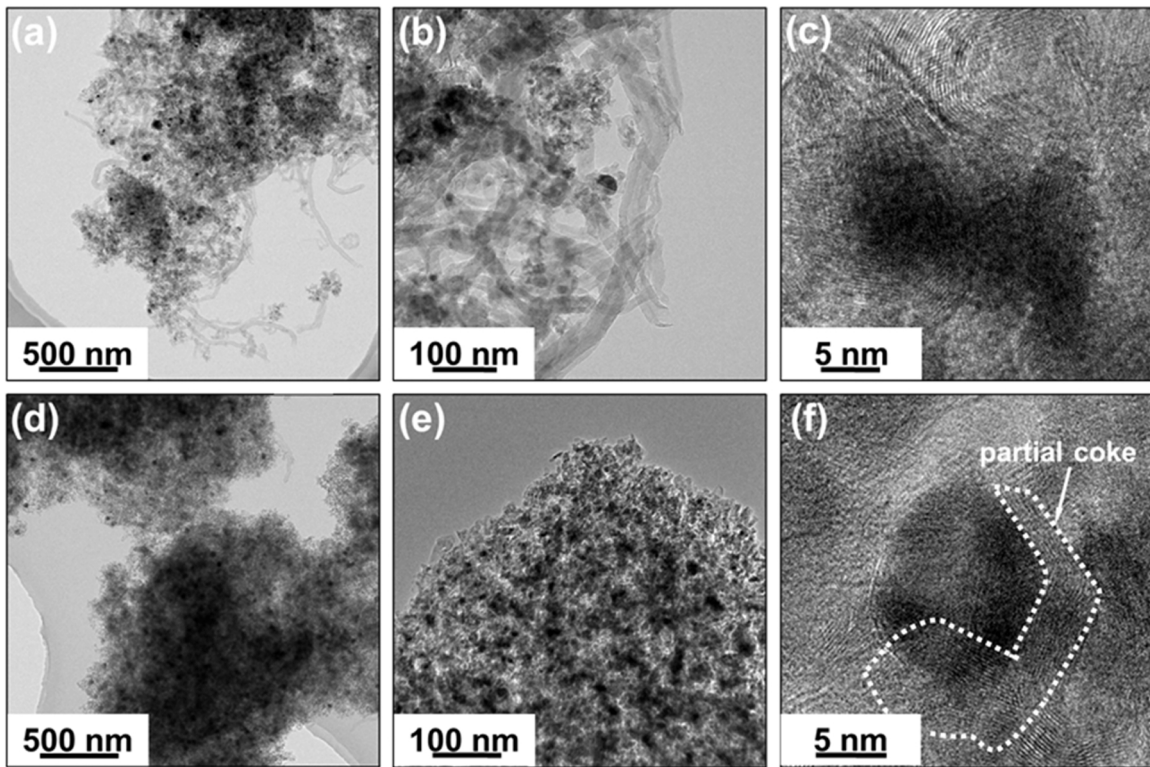


Fig. 4. TEM images of the spent (a, b, c) $\text{Ni}_3\text{Fe}_1/\text{Al}_2\text{O}_3$ and (d, e, f) $\text{Ni}_1\text{Fe}_1/\text{Al}_2\text{O}_3$ after 600 °C in DRM.

exhibited same morphology with bright Ni–Fe alloy particles highly dispersed on rod-like support (approximate 10 nm of width and 50 nm of length). The average Ni–Fe alloy particle size on $\text{Ni}_3\text{Fe}_1/\text{Al}_2\text{O}_3$ and $\text{Ni}_1\text{Fe}_1/\text{Al}_2\text{O}_3$ was 11.7 and 12.0 nm according to TEM analyses, respectively (Fig. S2). The two catalysts possessed similar particle size of Ni–Fe alloy, which suggests the minimum influence of particle size for the alloy in different catalytic performance. HRTEM images together with fast Fourier transform (FFT) analyses, as shown in Fig. 2d and h, reveal that different Ni–Fe alloys were formed on the two catalysts, where the well-defined lattice fringes of 0.205 and 0.180 nm were associated with Ni_3Fe_1 (111) and (200) planes, and that of 0.207 nm was ascribed to Ni_1Fe_1 (111) plane. EDS line scanning and mapping measurements were used to further illustrate the Ni–Fe alloy structures on $\text{Ni}_3\text{Fe}_1/\text{Al}_2\text{O}_3$ and $\text{Ni}_1\text{Fe}_1/\text{Al}_2\text{O}_3$ in Fig. 2e, f, i and j. The line scanning analysis for a representative Ni–Fe alloy particle (Fig. 2e and i) reveals that Ni and Fe elements displayed homogeneous distribution on the two

catalysts and the only difference was the intensity of Ni to Fe ratio, which is about 3:1 for Ni_3Fe_1 alloy and 1:1 for Ni_1Fe_1 alloy on Al_2O_3 . The EDS mapping analysis also confirms the uniform feature of as-obtained Ni–Fe alloys, as further illustrated by the consistent element patterns of green (Ni) and red (Fe) on one individual Ni–Fe particle (Fig. 2f and j).

3.3. Characterizations of Ni–Fe alloy catalysts after DRM

The structure investigation of the spent $\text{Ni}_3\text{Fe}_1/\text{Al}_2\text{O}_3$ and $\text{Ni}_1\text{Fe}_1/\text{Al}_2\text{O}_3$ catalysts was carried out by using XRD and aberration-corrected HAADF-STEM techniques. Fig. 3a and b show the XRD patterns of the spent $\text{Ni}_3\text{Fe}_1/\text{Al}_2\text{O}_3$ and $\text{Ni}_1\text{Fe}_1/\text{Al}_2\text{O}_3$, and the diffraction patterns of the spent catalysts were not identical to those of Ni–Fe alloys after reduction. For the spent $\text{Ni}_3\text{Fe}_1/\text{Al}_2\text{O}_3$, the peaks at 44.5°, 51.8° and 76.4° appeared, which was identified for the presence of metallic Ni^0 (PDF No. 87–0712). For the spent $\text{Ni}_1\text{Fe}_1/\text{Al}_2\text{O}_3$, the peaks for Ni_1Fe_1 alloy

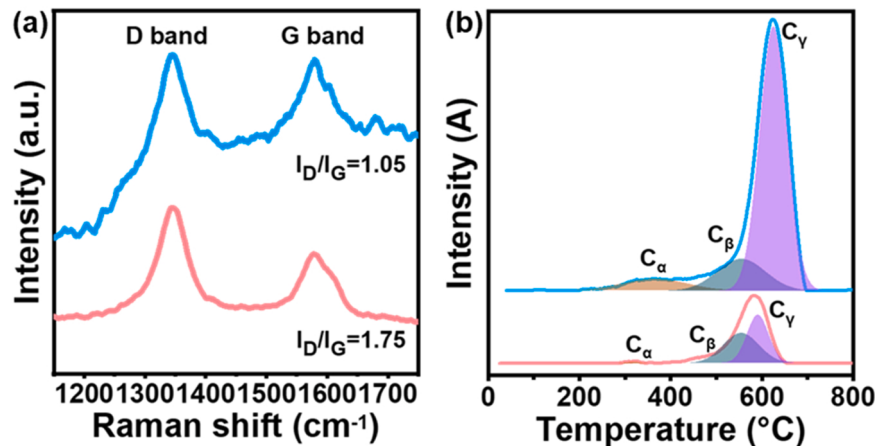


Fig. 5. (a) Raman spectra and (b) O_2 -TPO profiles of the spent $\text{Ni}_3\text{Fe}_1/\text{Al}_2\text{O}_3$ (blue) and $\text{Ni}_1\text{Fe}_1/\text{Al}_2\text{O}_3$ (pink) after DRM at 600 °C.

disappeared as accompanied by the generation of the peaks for Ni₃Fe₁ alloy. This indicates that the Ni–Fe alloy structures in Ni₃Fe₁/Al₂O₃ and Ni₁Fe₁/Al₂O₃ were reconstructed during the reaction. Besides, compared to the spent Ni₁Fe₁/Al₂O₃, on the XRD pattern of the spent Ni₃Fe₁/Al₂O₃, obvious diffraction peak at 2θ of 26.2° (with star mark) was observed, corresponding to the formation of crystalline carbonaceous species (002 plane).

The structure changes of Ni–Fe alloys on the spent Ni₃Fe₁/Al₂O₃ and Ni₁Fe₁/Al₂O₃ were then investigated by electron microscope analyses as shown in Fig. 3c, d, g and h. No aggregation of metal particle was detected on the two spent catalysts (Fig. 3c and g), as evidenced by the average size of small particles on the spent Ni₃Fe₁/Al₂O₃ (11.9 nm) and Ni₁Fe₁/Al₂O₃ (13.0 nm) (Fig. S2). The well-defined lattice fringes on the spent Ni₃Fe₁/Al₂O₃ and Ni₁Fe₁/Al₂O₃ were identified as 0.203 and 0.205 nm, which belonged to the formation of Ni (111) and Ni₃Fe₁ (111) planes, respectively (Fig. 3d and h). The experience of structural evolution on the spent Ni₃Fe₁/Al₂O₃ and Ni₁Fe₁/Al₂O₃ was also confirmed by EDS line scanning and mapping analyses (Fig. 3e, f, i and j). Only Ni element was detected on a representative particle on the spent Ni₃Fe₁/Al₂O₃ (Fig. 3e), and an obvious deficiency of Fe element was observed in the spent catalyst in comparison with that of Ni₃Fe₁/Al₂O₃ before reaction (Fig. 2e). However, Ni and Fe elements presented uniform distribution on a representative particle for the spent Ni₁Fe₁/Al₂O₃ in Fig. 3i. Impressively, compared to Ni₁Fe₁/Al₂O₃ after reduction, the intensity of Ni to Fe ratio increased to about 3:1. The results are well in line with the finding of EDS mapping in Fig. 3f and j, where the segregation of Fe from Ni–Fe alloys to supports exists, leading to the formation of Ni particle and Ni₃Fe₁ alloy on the spent Ni₃Fe₁/Al₂O₃ and Ni₁Fe₁/Al₂O₃ catalysts, respectively.

3.4. Carbon deposition on the spent Ni–Fe alloy catalysts after DRM

To further check the overall morphology, structure and amount of the deposited carbonaceous species on the spent catalysts, transmission electron microscopy (TEM), Raman spectroscopy and O₂ temperature programmed oxidation (O₂-TPO) measurements were performed, and the results are illustrated in Figs. 4 and 5. Fig. 4 shows the TEM images of the spent Ni₃Fe₁/Al₂O₃ and Ni₁Fe₁/Al₂O₃. Apparently, large quantities of carbon filaments were produced on the spent Ni₃Fe₁/Al₂O₃ in Fig. 4a, and some Ni particles were located on the top or inside these filaments in Fig. 4b. Furthermore, representative carbon onions existed and covered the surface of Ni particles in HRTEM analysis (Fig. 4c). However, only a small amount of carbon filaments was observed on the spent Ni₁Fe₁/Al₂O₃ through careful observation (Fig. 4d and e). In addition, the carbonaceous species (minor coke deposition) were partially grown on the Ni–Fe alloy particles of the spent Ni₁Fe₁/Al₂O₃ in HRTEM analysis (Fig. 4f).

Fig. 5a shows the Raman spectra of the spent Ni₃Fe₁/Al₂O₃ and Ni₁Fe₁/Al₂O₃. Two peaks appear at 1348 and 1596 cm⁻¹, which is indicative of D (imperfection of graphite) and G (graphite layers) bands of carbon deposition. The intensity ratio of D to G band (I_D/I_G) is normally used to evaluate the crystalline feature of carbonaceous species. A high I_D/I_G ratio refers to a lower crystalline order of carbonaceous species, where the I_D/I_G ratio was 1.05 for the spent Ni₃Fe₁/Al₂O₃ and 1.75 for the spent Ni₁Fe₁/Al₂O₃, which suggestss that carbonaceous species with lower graphitization were deposited on the latter in comparison with those on the former. We further calculated the amount of carbonaceous species on the two spent catalysts from thermogravimetry (TG) analysis as shown in Fig. S3a. The spent Ni₁Fe₁/Al₂O₃ presented a less amount of carbon deposition of 9.2% compared to that of 32.1% on the spent Ni₃Fe₁/Al₂O₃. Therefore, carbon deposition rate on the spent Ni₃Fe₁/Al₂O₃ was 9.45 mg_C g_{cat}⁻¹ h⁻¹, which is about 4.7 times larger than that of 2.03 mg_C g_{cat}⁻¹ h⁻¹ on the spent Ni₁Fe₁/Al₂O₃.

Fig. 5b presents O₂-TPO profiles of the spent two catalysts and the distinct carbonaceous species were determined by different oxidation temperature. The spent Ni₃Fe₁/Al₂O₃ possessed the peaks at 365, 555,

Table 1

The oxidation temperature and different ratios of carbonaceous species on the spent Ni₃Fe₁/Al₂O₃ and Ni₁Fe₁/Al₂O₃.

Catalyst	Temperature (°C)			Proportion (%)		
	C _α	C _β	C _γ	C _α	C _β	C _γ
the spent Ni ₃ Fe ₁ /Al ₂ O ₃	365	555	625	7.8	16.0	76.2
the spent Ni ₁ Fe ₁ /Al ₂ O ₃	318	555	591	1.6	49.9	48.5

and 625 °C and the spent Ni₁Fe₁/Al₂O₃ exhibited the peaks at 318, 555, and 591 °C, which were originated from the presence of active carbon atoms (C_α), less active carbon species (C_β) and inactive coke species (C_γ), respectively. [30–32] The oxidation temperature of carbon deposition on the spent Ni₃Fe₁/Al₂O₃ were higher than those of the spent Ni₁Fe₁/Al₂O₃ (Table 1), indicating the formation of more carbon species with less reactivity on the former than those on the latter. Meanwhile, C_γ species (coke deposition) on the spent Ni₃Fe₁/Al₂O₃ accounted for 76.2% of the carbon deposition, which is higher than those of 48.5% on the spent Ni₁Fe₁/Al₂O₃. It is therefore should be noted that less carbon species with lower graphitization (more active carbon species) were generated on the spent Ni₁Fe₁/Al₂O₃ compared to those on the spent Ni₃Fe₁/Al₂O₃.

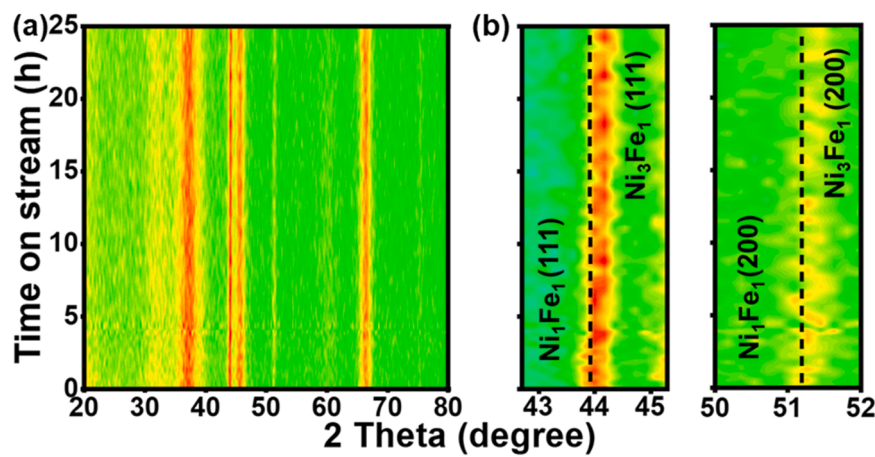
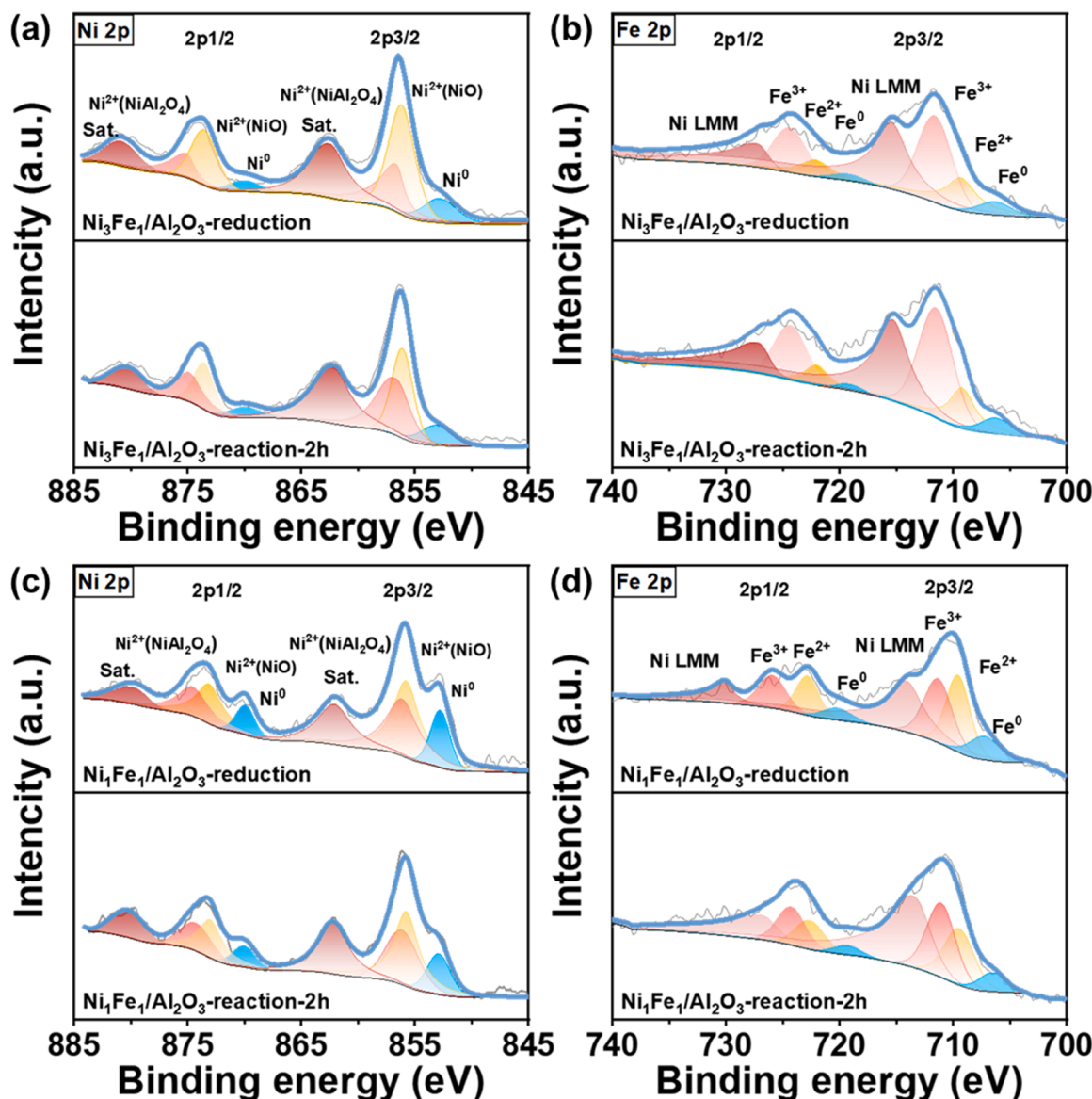
4. Discussions

4.1. Structure evolution of Ni₃Fe₁/Al₂O₃ and Ni₁Fe₁/Al₂O₃ in DRM

To get deeper insights into the structure changes of the Ni–Fe alloys on Ni₃Fe₁/Al₂O₃ and Ni₁Fe₁/Al₂O₃, *in situ* XRD experiments were used to monitor the evolution of the alloy structure during DRM. For Ni₃Fe₁/Al₂O₃, the diffraction peaks assigned to Ni₃Fe₁ (111) and (200) alloy shifted to higher 2θ values from 44.2° and 51.5° to 44.5° and 51.8°, separately, when the Ni₃Fe₁ alloy catalyst was exposed to the reactants for 0.5 h (Fig. S4). This confirms that Ni₃Fe₁ alloy changes to metallic Ni particles on Ni₃Fe₁/Al₂O₃ during DRM owing to the quick segregation of Fe from the surface of alloy particles. Furthermore, the peaks for Ni particles could not be detected during the test for about 1 h (the measurement was shut off), which is originated from the bulge of the sample in the reaction cell due to formation of coke (as illustrated in Fig. S5). However, for Ni₁Fe₁/Al₂O₃, the diffraction peaks for Ni₁Fe₁ (111) and (200) alloy shifted to higher 2θ values from 43.9° to 44.2° for (111) plane and from 51.2° to 51.5° for (200) plane, separately. This indicates that the structure transformation from Ni₁Fe₁ alloy generally to Ni₃Fe₁ alloy existed during the reaction (Fig. 6a), which could be further confirmed by the clearly increased 2θ values of the peaks for (111) and (200) planes, as shown in Fig. 6b.

It should be mentioned that no obvious oxidized Fe species were observed on the two catalysts during *in situ* XRD analyses. The result is well matched with previous findings that the formation of very small domains of FeO_x [20] or the presence of intermediate phase of FeO species strongly depended on reaction temperature and gas composition [18]. We further performed *in situ* X-ray photoelectron spectroscopy (XPS) to determine the formation and evolution of FeO_x species, as shown in Fig. 7 and Table S1. Besides the presence of NiO and NiAl₂O₄, metallic Ni⁰ and Fe⁰ appeared and verified the formation of Ni–Fe alloy of the two catalysts after *in situ* reduction under H₂ for 1 h (Fig. 7). The ratios of Ni⁰ to Fe⁰ on the surface of Ni₃Fe₁/Al₂O₃ and Ni₁Fe₁/Al₂O₃ were approximate 2.76 and 1.10, respectively (Fig. 7a and b). In addition, the ratios of Fe⁰ to Feⁿ⁺ (n = 2 and 3) on the surface of Ni₃Fe₁/Al₂O₃ and Ni₁Fe₁/Al₂O₃ were 0.13 and 0.20, respectively (Fig. 7c).

Notably, for Ni₃Fe₁/Al₂O₃, the ratio of Ni⁰ to Fe⁰ increased to 3.13 for 2 h reaction, accompanied by the decrease of the ratio of Fe⁰ to Feⁿ⁺ to 0.09 under reaction condition. For Ni₁Fe₁/Al₂O₃, the ratio of Ni⁰ to Fe⁰ changed to 1.37 for 2 h reaction, and the ratio of Fe⁰ to Feⁿ⁺ were 0.14 under reaction for 2 h (Fig. 7d). It should be noticed that the ratio

Fig. 6. In situ XRD patterns of Ni₁Fe₁/Al₂O₃ at 600 °C in DRM.Fig. 7. In situ XPS spectra of (a, b) Ni₃Fe₁/Al₂O₃ and (c, d) Ni₁Fe₁/Al₂O₃ after in situ reduction and reaction for 2 h in DRM.

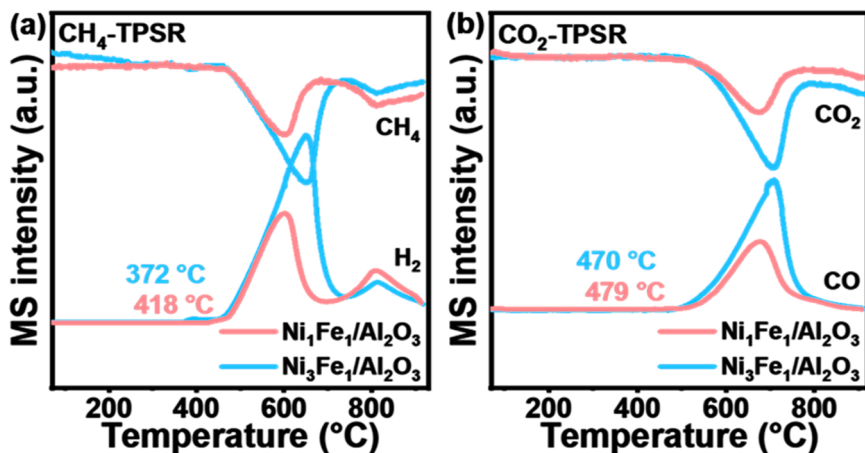


Fig. 8. (a) CH₄-TPSR and (b) CO₂-TPSR profiles of Ni₃Fe₁/Al₂O₃ and Ni₁Fe₁/Al₂O₃ from 50 to 800 °C and maintained at 800 °C for another 11 min.

of Fe⁰ to Feⁿ⁺ decreased on Ni–Fe alloys during DRM, whereas the ratio of Ni⁰ to Ni²⁺ remained unchanged (Table S1). This reveals that the growth of small FeO_x existed on the surface of Ni–Fe alloys on the two alloy catalysts during the reaction. Meanwhile, stable Ni–Fe alloy was achieved by the reaction FeO_x and active carbon species to regenerate Fe⁰ and CO (Eq. 5). The alloy on Ni₃Fe₁/Al₂O₃ would separate into metallic Ni and FeO_x on Al₂O₃ (Eq. 4) as evidenced by the larger Ni⁰/Fe⁰ ratio and smaller Fe⁰/Feⁿ⁺ ratio in comparison with those of Ni₁Fe₁/Al₂O₃ after reaction. Therefore, for Ni₃Fe₁/Al₂O₃, large amounts of inactive carbon species (major coke deposition) retarded the reaction with FeO_x to form Fe⁰ and CO, leading to the occurrence through a facile and severe dealloy process. However, for Ni₁Fe₁/Al₂O₃, sufficient amounts of Fe⁰ in the equimolar alloy provided enough resources for segregation of Fe during the dealloying process. In addition, partial FeO_x could react with low crystalline carbon species to realloy into Fe⁰ during DRM, as confirmed by the formation of Ni₃Fe₁ alloy through in situ XRD analysis (Fig. 6).

4.2. Temperature programmed surface reaction on Ni–Fe alloy catalysts

Generally, the particle size of Ni-based alloy catalysts has a profound influence on carbon deposition rate and different carbon species. However, Ni₃Fe₁/Al₂O₃ and Ni₁Fe₁/Al₂O₃ catalysts presented similar average particle size and size distribution before and after the reaction (Fig. S2). It is therefore reasonable to rule out the effect of particle size and dispersion on the distinct carbon deposition. To further study the reactivity towards CH₄ or CO₂ activation over Ni–Fe alloy catalysts, CH₄ or CO₂ temperature programmed surface reaction (TPSR) were carried out and mass signals of CH₄, H₂, CO₂ and CO are recorded in Fig. 8. For CH₄-TPSR, the first starting temperature for H₂ formation related to initial temperature of CH₄ activation on Ni₃Fe₁/Al₂O₃ and Ni₁Fe₁/Al₂O₃ were 372 and 418 °C, respectively. For CO₂-TPSR, the associated CO₂ activation temperature for Ni₃Fe₁/Al₂O₃ and Ni₁Fe₁/Al₂O₃ occurred at 470 and 479 °C, respectively. Clearly, the two Ni–Fe alloy catalysts exhibited similar onset temperature for CO₂ activation, but different onset temperature and temperature range for CH₄ activation. This suggests that CO₂ activation experienced in similar manner over the two catalysts but CH₄ was more prone to dissociate into carbonaceous species on Ni₃Fe₁/Al₂O₃ (temperature window from 460° to 731 °C) in comparison with that on Ni₁Fe₁/Al₂O₃ (temperature window from 473° to 668 °C).

Besides, a small peak appears on CH₄-TPSR profiles of the two catalysts. The onset temperature for the second peak started at 751 and 710 °C for Ni₃Fe₁/Al₂O₃ and Ni₁Fe₁/Al₂O₃, respectively, which belongs to CH₄ dissociation on Fe⁰ in Ni–Fe alloy. [33–35] We further evaluated the stability of Ni₃Fe₁/Al₂O₃ and Ni₁Fe₁/Al₂O₃ catalysts at 700 °C as

shown in Fig. S6. CH₄ and CO₂ conversions of Ni₃Fe₁/Al₂O₃ were 69% and 80% for 50 h; whereas the activity of Ni₁Fe₁/Al₂O₃ declined from 62% to 46% for CH₄ conversion and from 75% to 62% for CO₂ conversion with time on stream. The final H₂/CO ratio was 0.88 and 0.70 for Ni₃Fe₁/Al₂O₃ and Ni₁Fe₁/Al₂O₃.

It can be seen that the two spent catalysts had large amounts of crystalline coke after 700 °C, as evidenced by the presence of obvious carbon diffraction peak at 26.2° in XRD patterns (Fig. S7). The amounts of carbon deposition on the spent Ni₃Fe₁/Al₂O₃ and Ni₁Fe₁/Al₂O₃ were 57.8% and 37.4% after 700 °C (Fig. S3b), respectively, which is higher than those of the corresponding spent catalysts after 600 °C. This suggests that Fe⁰ in Ni–Fe alloy performed as new sites for CH₄ dissociation, which inversely lead to the increased tendency for coke deposition. A considerable number of carbon filaments were observed on the two spent catalysts (Fig. S8), and metallic Ni particles with severe segregation behavior on the alloys were grown on the top of carbon filaments on the spent Ni₃Fe₁/Al₂O₃ and Ni₁Fe₁/Al₂O₃ catalysts (Fig. S9 and S10). Therefore, the intimate interaction between Ni and Fe on robust Ni₃Fe₁ alloy from iron-surplus induced method is favorable to improve the coke resistance by Mars–van Krevelen (MvK) mechanism at 600 °C. However, high temperature reaction plays a detrimental and notorious role for the alloy catalysts, leading to the formation of large amounts of coke (carbon filaments).

Owing to the good stability of Ni–Fe alloy on Ni₁Fe₁/Al₂O₃, we carried out kinetic studies of Ni₁Fe₁/Al₂O₃ in DRM to determine reaction order and activation energy. Under the kinetic control, the order of reaction of CH₄ was 0.92, which was higher than that of CO₂ for 0.31 (Fig. S11, detailed calculation is shown in supporting information). This indicates that the changing partial pressure of CH₄ has a larger influence than that of CO₂ on Ni₁Fe₁/Al₂O₃. The activation energy of CH₄ and CO₂ are nearly comparable as 153 and 165 kJ mol⁻¹, respectively. In addition, compared with other Ni–Fe catalysts (Table S2), Ni₁Fe₁/Al₂O₃ presented distinct performance without the decline of CH₄ and CO₂ conversions for 50 h, and relatively low carbon deposition rate with low crystalline amorphous carbon species.

4.3. Reaction pathway for enhanced performance on Ni–Fe alloy catalysts

In order to dig deeper insight into the distinct catalytic behaviors of Ni₃Fe₁/Al₂O₃ and Ni₁Fe₁/Al₂O₃, in situ Fourier transform infrared (FTIR) spectroscopy was carried out to monitor the reaction intermediates in DRM at 600 °C (Fig. 9). Both catalysts possessed gaseous peaks at 3016 and 1305 cm⁻¹ for CH₄, at 2356 and 2308 cm⁻¹ for CO₂, and at 2186 and 2104 cm⁻¹ for CO as shown in Fig. 9a and c. For Ni₃Fe₁/Al₂O₃, three key intermediates were detected in the IR fingerprint region

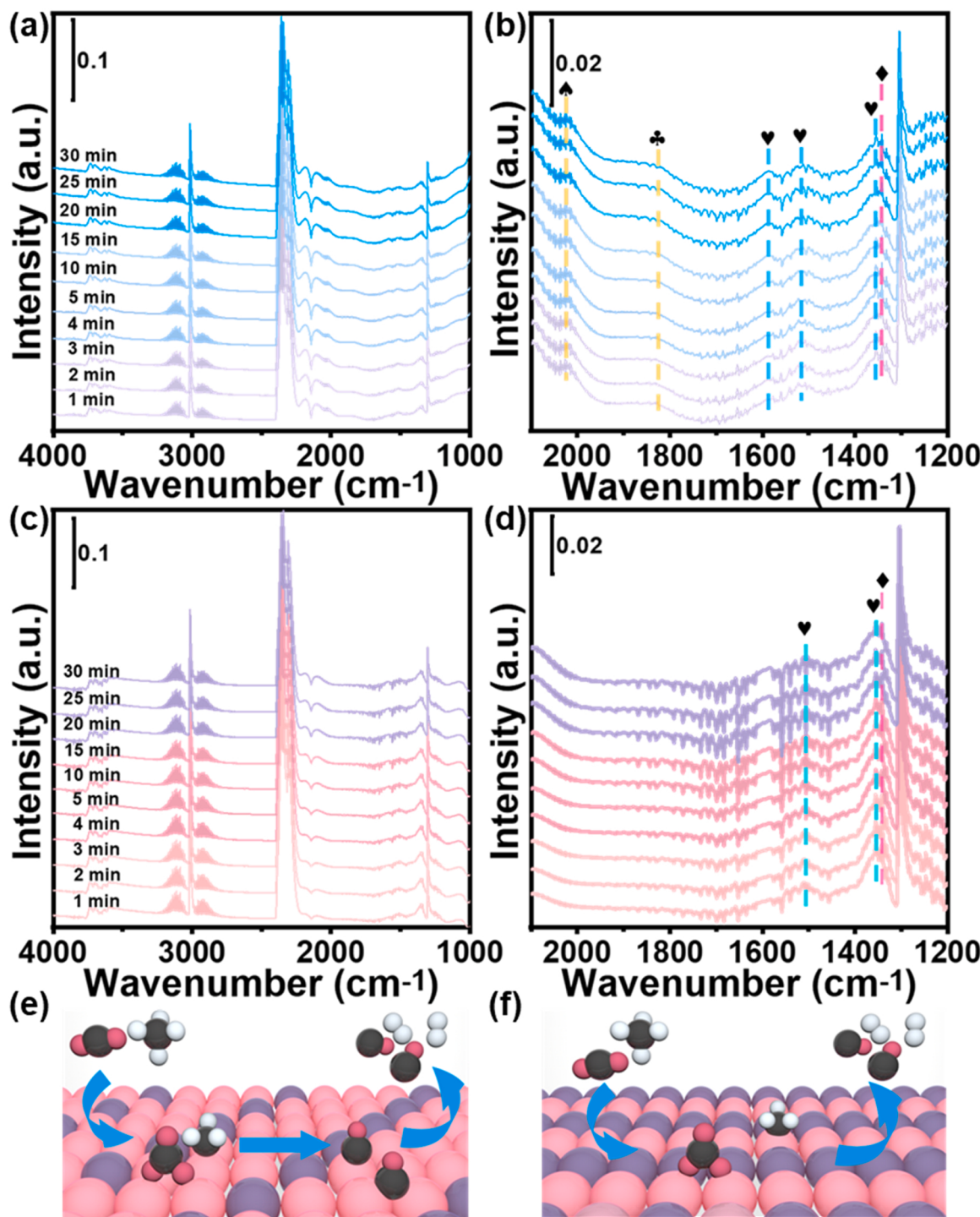


Fig. 9. In situ FTIR spectra of (a, b) $\text{Ni}_3\text{Fe}_1/\text{Al}_2\text{O}_3$ and (c, d) $\text{Ni}_1\text{Fe}_1/\text{Al}_2\text{O}_3$ at 600 °C. ♠, ♦, ♥ and ♦ represent linearly adsorbed $^*\text{CO}$, bridged adsorbed $^*\text{CO}$, carbonate species and $^*\text{CH}_3$, respectively. The evolution of reaction intermediates of (e) $\text{Ni}_3\text{Fe}_1/\text{Al}_2\text{O}_3$ and (f) $\text{Ni}_1\text{Fe}_1/\text{Al}_2\text{O}_3$ during DRM.

from 1200 to 2100 cm^{-1} , as shown in Fig. 9b. The first presented observable peaks at 1355, 1517 and 1587 cm^{-1} , which are attributed to the presence of carbonate species. [36–39] The second was determined by the presence of CH_4 dissociated species ($^*\text{CH}_3$), as evidenced by the peak observed at 1342 cm^{-1} [2] [40–42]. The third was identified as chemisorbed $^*\text{CO}$ species, and exhibited peaks at 2023 and 1826 cm^{-1} , which are ascribed to the linearly and bridged adsorbed on Ni, respectively. [43,44] For $\text{Ni}_1\text{Fe}_1/\text{Al}_2\text{O}_3$, only carbonate and $^*\text{CH}_3$ species appeared at 1510/1355 and 1342 cm^{-1} , respectively, as key important reaction intermediates during DRM (Fig. 9d). The absence of linearly or

bridged adsorbed $^*\text{CO}$ on $\text{Ni}_1\text{Fe}_1/\text{Al}_2\text{O}_3$ suggests the facile desorption of CO to gaseous product. CO temperature-programmed desorption (TPD) was used to study the CO adsorbed ability on the two catalysts (Fig. S12). The desorption temperatures of weakly and strongly bonding CO on $\text{Ni}_3\text{Fe}_1/\text{Al}_2\text{O}_3$ (199 and 374 °C) were higher than those on $\text{Ni}_1\text{Fe}_1/\text{Al}_2\text{O}_3$ (185 and 327 °C). This indicates CO is more stronger binding with the alloy particle on the former than the latter. In addition, the temperature window of the TPD profile for $\text{Ni}_3\text{Fe}_1/\text{Al}_2\text{O}_3$ started from 50 to 616 °C, while the temperature window of the profile of $\text{Ni}_1\text{Fe}_1/\text{Al}_2\text{O}_3$ was in the range from 50 to 570 °C. CO desorption signal

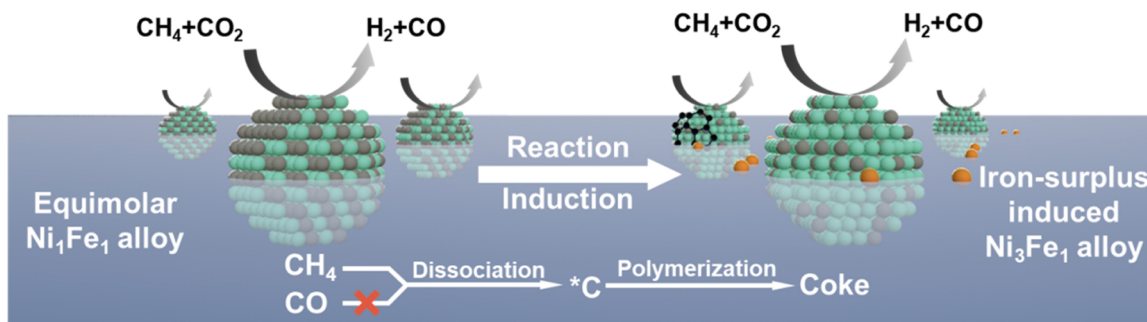


Fig. 10. Schematic illustration of the iron-surplus strategy to design stable Ni_3Fe_1 alloy over Al_2O_3 from the equimolar Ni_1Fe_1 alloy during DRM at 600 °C. Green and black particles represent Ni and Fe atoms, and yellow particles refer to FeO_x species.

was not observed on the profile of $\text{Ni}_1\text{Fe}_1/\text{Al}_2\text{O}_3$ after 600 °C. This result is well matched with the findings of in situ FTIR that CO and CH_4 dissociation concurrently occurred on $\text{Ni}_3\text{Fe}_1/\text{Al}_2\text{O}_3$, while only CH_4 dissociation appeared on $\text{Ni}_1\text{Fe}_1/\text{Al}_2\text{O}_3$. Generally, CO and CH_4 dissociation (Eqs. 2 and 3) are the main origins for coke deposition on Ni catalysts, which had a detrimental effect on catalytic stability. [6,45] The two Ni–Fe alloy catalysts had distinct pathways for coke deposition, which was originated from CO and CH_4 dissociation on the directly reduced $\text{Ni}_3\text{Fe}_1/\text{Al}_2\text{O}_3$ (Fig. 9e), but was mainly attributed to CH_4 dissociation on the iron-surplus induced $\text{Ni}_3\text{Fe}_1/\text{Al}_2\text{O}_3$ from the equimolar $\text{Ni}_1\text{Fe}_1/\text{Al}_2\text{O}_3$ (Fig. 9f).

Overall, the proposed reaction pathways for $\text{Ni}_3\text{Fe}_1/\text{Al}_2\text{O}_3$ and $\text{Ni}_1\text{Fe}_1/\text{Al}_2\text{O}_3$ are illustrated in Fig. S13 and Fig. 10 on the basis of the results from in situ XRD, in situ FTIR, carbon deposition analyses and stability test. Two Ni–Fe alloys catalysts were developed to resolve the bottleneck issue of coke deposition for DRM. $\text{Ni}_3\text{Fe}_1/\text{Al}_2\text{O}_3$ had additional pathway for coke deposition, including CO and CH_4 dissociation, in comparison with that of only CH_4 dissociation on $\text{Ni}_1\text{Fe}_1/\text{Al}_2\text{O}_3$, which results to larger amounts of coke deposition (76.2% and 48.5% C_γ species on $\text{Ni}_3\text{Fe}_1/\text{Al}_2\text{O}_3$ and $\text{Ni}_1\text{Fe}_1/\text{Al}_2\text{O}_3$) alongside higher crystalline of coke (at 625 and 591 °C for $\text{Ni}_3\text{Fe}_1/\text{Al}_2\text{O}_3$ and $\text{Ni}_1\text{Fe}_1/\text{Al}_2\text{O}_3$) on the former than those on the latter.

It has been extensively accepted that Ni–Fe alloy plays a crucial important role for an enhanced coke-resistant property by carbon gasification route on FeO_x from Eq. 5 [18–20]. The main origin for the coke deposition could be traced to the dealloying process as evidenced by the segregation of Fe from Ni–Fe alloy particles. For $\text{Ni}_3\text{Fe}_1/\text{Al}_2\text{O}_3$, FeO_x that would not realloy into the alloy structure, separated from the alloy particle and migrated into the support matrix, which leading to the generation of Ni particles and insufficient ability to remove the deposited carbonaceous species and further to coke (Fig. S13). However, for $\text{Ni}_1\text{Fe}_1/\text{Al}_2\text{O}_3$ (Fig. 10), owing to the iron-surplus strategy, stable Ni_3Fe_1 alloy over Al_2O_3 was achieved regardless of the segregation of Fe from Ni_1Fe_1 alloy, which would maintain enough FeO_x closed interacted with Ni [18] and realloy into the robust $\text{Ni}_3\text{Fe}_1/\text{Al}_2\text{O}_3$ during DRM reaction.

5. Conclusion

In this study, to resolve the bottleneck issue of coke deposition of Ni–Fe alloy catalysts by the existence of Fe segregation, $\text{Ni}_1\text{Fe}_1/\text{Al}_2\text{O}_3$ and $\text{Ni}_3\text{Fe}_1/\text{Al}_2\text{O}_3$ with different Ni–Fe alloy structures were synthesized by using an evaporation-induced self-assembly approach. $\text{Ni}_1\text{Fe}_1/\text{Al}_2\text{O}_3$ presented distinct catalytic behavior for DRM in comparison with that of $\text{Ni}_3\text{Fe}_1/\text{Al}_2\text{O}_3$. The final CH_4 and CO_2 conversions on $\text{Ni}_1\text{Fe}_1/\text{Al}_2\text{O}_3$ were 28% and 40%, which were higher than those of 18% and 30% on $\text{Ni}_3\text{Fe}_1/\text{Al}_2\text{O}_3$ at 600 °C for 50 h. Notably, H_2 directly reduced Ni_3Fe_1 alloy changed to Ni particle and FeO_x owing to the dealloying process; however, Ni_1Fe_1 alloy gradually transformed into Ni_3Fe_1 alloy during DRM reaction at 600 °C. The surplus Fe in the equimolar Ni_1Fe_1 alloy not only provided sufficient resources for Fe segregation during the

dealloying process, but also significantly reduced the amount and graphitization of coke deposition. The origin of coke formation on the dealloying $\text{Ni}/\text{Al}_2\text{O}_3$ from $\text{Ni}_3\text{Fe}_1/\text{Al}_2\text{O}_3$ was found from CO and CH_4 dissociation, whereas the reason for coke formation on the iron-surplus induced $\text{Ni}_3\text{Fe}_1/\text{Al}_2\text{O}_3$ from $\text{Ni}_1\text{Fe}_1/\text{Al}_2\text{O}_3$ was only caused by CH_4 dissociation as confirmed by in situ FTIR analyses.

CRediT authorship contribution statement

Yubin Li: Methodology, Validation, Formal analysis, Investigation, Data curation, Writing – original draft. **Qianqian Wang:** Methodology, Formal analysis, Investigation, Writing – original draft. **Min Cao:** Methodology, Investigation. **Sha Li:** Conceptualization, Investigation, Formal analysis, Writing – review & editing, Project administration. **Zhiwen Song:** Methodology, Data curation. **Li Qiu:** Investigation. **Feng Yu:** Methodology. **Ruifeng Li:** Resources, Supervision, Funding acquisition. **Xiaoliang Yan:** Conceptualization, Methodology, Resources, Writing – review & editing, Supervision.

Declaration of Competing Interest

The authors declare that they have no known competing financial interests or personal relationships that could have appeared to influence the work reported in this paper.

Data Availability

Data will be made available on request.

Acknowledgements

The authors acknowledge the National Natural Science Foundation of China (Nos. 22278286, 22108189, 21878203), Shanxi-Zheda Institute of Advanced Materials and Chemical Engineering (2021SX-TD005), and the Program for the Top Young and Middle-aged Innovative Talents of Higher Learning Institutions of Shanxi.

Appendix A. Supporting information

Supplementary data associated with this article can be found in the online version at doi:10.1016/j.apcatb.2023.122669.

References

- [1] D.D. Wang, P. Littlewood, T.J. Marks, P.C. Stair, E. Weitz, Coking can enhance product yields in the dry reforming of methane, *ACS Catal.* 12 (2022) 8352–8362.
- [2] Q.Q. Wang, W. Wang, M. Cao, S. Li, P.F. Wang, J.Q. He, R.F. Li, X.L. Yan, Effect of interstitial carbon atoms in core–shell $\text{Ni}_3\text{ZnC}_{0.7}/\text{Al}_2\text{O}_3$ catalyst for high-performance dry reforming of methane, *Appl. Catal. B: Environ.* 317 (2022) 121806.
- [3] M. Akri, S. Zhao, X.Y. Li, K.T. Zang, A.F. Lee, M.A. Isaacs, W. Xi, Y. Gangarajula, J. Luo, Y.J. Ren, Y.T. Cui, L. Li, Y. Su, X.L. Pan, W. Wen, Y. Pan, K. Wilson, L. Li, B.

T. Qiao, H. Ishii, Y.F. Liao, A.Q. Wang, X.D. Wang, T. Zhang, Atomically dispersed nickel as coke-resistant active sites for methane dry reforming, *Nat. Commun.* 10 (2019) 5181.

[4] S. Joo, K. Kim, O. Kwon, J. Oh, H.J. Kim, L.J. Zhang, J. Zhou, J.Q. Wang, H.Y. Jeong, J.W. Han, G. Kim, Enhancing thermocatalytic activities by upshifting the d-band center of exsolved Co–Ni–Fe ternary alloy nanoparticles for the dry reforming of methane, *Angew. Chem. Int. Ed.* 60 (2021) 15912–15919.

[5] T. Margossian, K. Larmier, S.M. Kim, F. Krumeich, A. Fedorov, P. Chen, C.R. Muller, C. Coperet, Molecularly tailored nickel precursor and support yield a stable methane dry reforming catalyst with superior metal utilization, *J. Am. Chem. Soc.* 139 (2017) 6919–6927.

[6] X.L. Yan, T. Hu, P. Liu, S. Li, B.R. Zhao, Q. Zhang, W.Y. Jiao, S. Chen, P.F. Wang, J. Lu, L.M. Fan, X.N. Deng, Y.X. Pan, Highly efficient and stable Ni/CeO₂-SiO₂ catalyst for dry reforming of methane: effect of interfacial structure of Ni/CeO₂ on SiO₂, *Appl. Catal. B: Environ.* 246 (2019) 221–231.

[7] J.H. Dong, Q. Fu, H.B. Li, J.P. Xiao, B. Yang, B.S. Zhang, Y.X. Bai, T.Y. Song, R.K. Zhang, L.J. Gao, J. Cai, H. Zhang, Z. Liu, X.H. Bao, Reaction-induced strong metal–support interactions between metals and inert boron nitride nanosheets, *J. Am. Chem. Soc.* 142 (2020) 17167–17174.

[8] S. Joo, A. Seong, O. Kwon, K. Kim, J.H. Lee, R.J. Gorte, J.M. Vohs, J.W. Han, G. Kim, Highly active dry methane reforming catalysts with boosted in situ grown Ni–Fe nanoparticles on perovskite via atomic layer deposition, *Sci. Adv.* 6 (2020) eabb1573.

[9] Y. Song, E. Ozdemir, S. Ramesh, A. Adishev, S. Subramanian, A. Harale, M. Albuali, B.A. Fahdel, A. Jamal, D. Moon, S.H. Choi, C.T. Yavuz, Dry reforming of methane by stable Ni–Mo nanocatalysts on single-crystalline MgO, *Science* 367 (2020) 777–781.

[10] H.C. Li, C. Hao, J.Q. Tian, S. Wang, C. Zhao, Ultra-durable Ni–Ir/MgAl₂O₄ catalysts for dry reforming of methane enabled by dynamic balance between carbon deposition and elimination, *Chem. Catal.* 2 (2022) 1748–1763.

[11] M. Torimoto, Y. Sekine, Effects of alloying for steam or dry reforming of methane: a review of recent studies, *Catal. Sci. Technol.* 12 (2022) 3387–3411.

[12] V. De Coster, N.V. Srinath, S.A. Theofanidis, A. Van Alboom, H. Poelman, M. K. Sabbe, G.B. Marin, V.V. Galvita, Looking inside a Ni–Fe/MgAl₂O₄ catalyst for methane dry reforming via Mossbauer spectroscopy and in situ QXAS, *Appl. Catal. B: Environ.* 300 (2022), 120720.

[13] M.S. Ferrandon, C. Byron, G. Celik, Y.Y. Zhang, C.Y. Ni, J. Sloppy, R.A. McCormick, K. Booksh, A.V. Teplyakov, M. Delferro, Grafted nickel-promoter catalysts for dry reforming of methane identified through high-throughput experimentation, *Appl. Catal. A: Gen.* 629 (2021), 118379.

[14] H.S. Bengaard, J.K. Nørskov, J. Sehested, B.S. Clausen, L.P. Nielsen, A. Molenbroek, J.R. Rostrup-Nielsen, Steam reforming and graphite formation on Ni catalysts, *J. Catal.* 209 (2002) 365–384.

[15] S. Helveg, C. Lopez-Cartes, J. Sehested, P.L. Hansen, B.S. Clausen, J.R. Rostrup-Nielsen, F. Abild-Pedersen, J.K. Nørskov, Atomic-scale imaging of carbon nanofibre growth, *Nature* 427 (2004) 426–429.

[16] T.T. Zhang, Z.X. Liu, Y.A. Zhu, Z.C. Liu, Z.J. Sui, K.K. Zhu, X.G. Zhou, Dry reforming of methane on Ni–Fe–MgO catalysts: Influence of Fe on carbon-resistant property and kinetics, *Appl. Catal. B: Environ.* 264 (2020), 118497.

[17] X.G. Zheng, S.Y. Tan, L.C. Dong, S.B. Li, H.M. Chen, Plasma-assisted catalytic dry reforming of methane: highly catalytic performance of nickel ferrite nanoparticles embedded in silica, *J. Power Sources* 276 (2015) 286–294.

[18] S.A. Theofanidis, V.V. Galvita, H. Poelman, G.B. Marin, Enhanced carbon-resistant dry reforming Fe–Ni catalyst: Role of Fe, *ACS Catal.* 5 (2015) 3028–3039.

[19] M.A. Serrer, A. Gaur, J. Jelic, S. Weber, C. Fritsch, A.H. Clark, E. Saraci, F. Studt, J. D. Grunwaldt, Structural dynamics in Ni–Fe catalysts during CO₂ methanation-role of iron oxide clusters, *Catal. Sci. Technol.* 10 (2020) 7542–7554.

[20] S.M. Kim, P.M. Abdala, T. Margossian, D. Hosseini, L. Foppa, A. Armutlulu, W. van Beek, A. Comas-Vives, C. Coperet, C. Muller, Cooperativity and dynamics increase the performance of NiFe dry reforming catalysts, *J. Am. Chem. Soc.* 139 (2017) 1937–1949.

[21] S.A. Theofanidis, R. Batchu, V.V. Galvita, H. Poelman, G.B. Marin, Carbon gasification from Fe–Ni catalysts after methane dry reforming, *Appl. Catal. B: Environ.* 185 (2016) 42–55.

[22] T. Margossian, K. Larmier, S.M. Kim, F. Krumeich, C. Muller, C. Coperet, Supported bimetallic NiFe nanoparticles through colloid synthesis for improved dry reforming performance, *ACS Catal.* 7 (2017) 6942–6948.

[23] L. Wang, D.L. Li, M. Koike, S. Koso, Y. Nakagawa, Y. Xu, K. Tomishige, Catalytic performance and characterization of Ni–Fe catalysts for the steam reforming of tar from biomass pyrolysis to synthesis gas, *Appl. Catal. A: Gen.* 392 (2011) 248–255.

[24] S.Q. Wang, X.C. Lan, B.Y. Liu, B. Ali, T.F. Wang, Boosting amination of 1-Octanol to 1-Octylamine via metal–metal oxide interactions in Ni_xFe₁/Al₂O₃ catalysts, *ChemCatChem* 14 (2022), e202101728.

[25] Z.W. Song, Q.Q. Wang, C. Guo, S. Li, W.J. Yan, W.Y. Jiao, L. Qiu, X.L. Yan, R.F. Li, Improved effect of Fe on the stable NiFe/Al₂O₃ catalyst in low-temperature dry reforming of methane, *Ind. Eng. Chem. Res.* 59 (2020) 17250–17258.

[26] A. Tsoukalou, Q. Imtiaz, S.M. Kim, P.M. Abdala, S. Yoon, C.R. Muller, Dry-reforming of methane over bimetallic Ni–M/La₂O₃ (M = Co, Fe): the effect of the rate of La₂O₂CO₃ formation and phase stability on the catalytic activity and stability, *J. Catal.* 343 (2016) 208–214.

[27] S.A. Theofanidis, V.V. Galvita, M. Sabbe, H. Poelman, C. Detavernier, G.B. Marin, Controlling the stability of a Fe–Ni reforming catalyst: structural organization of the active components, *Appl. Catal. B: Environ.* 209 (2017) 405–416.

[28] S. Shah, S. Sayono, J. Ynzunza, R. Pan, M.J. Xu, X.Q. Pan, K.L. Gilliard-AbdulAziz, The effects of stoichiometry on the properties of exsolved Ni–Fe alloy nanoparticles for dry methane reforming, *AIChE J.* 66 (2020), e17078.

[29] G. Gunduz-Meric, S. Kaytakoglu, L. Degirmenci, Catalytic performance of silica covered bimetallic nickel–iron encapsulated core–shell microspheres for hydrogen production, *Int. J. Hydrog. Energy* 45 (2020) 34547–34556.

[30] J.G. McCarty, H. Wise, Hydrogenation of surface carbon on alumina-supported nickel, *J. Catal.* 57 (1979) 406–416.

[31] J. Rostrup-Nielsen, D.L. Trimm, Mechanisms of carbon formation on nickel-containing catalysts, *J. Catal.* 48 (1977) 155–165.

[32] Z.L. Zhang, X.E. Verykios, Carbon dioxide reforming of methane to synthesis gas over supported Ni catalysts, *Catal. Today* 21 (1994) 589–595.

[33] M. Zhang, J.F. Zhang, Y.Q. Wu, J.X. Pan, Q.D. Zhang, Y.S. Tan, Y.Z. Han, Insight into the effects of the oxygen species over Ni/ZrO₂ catalyst surface on methane reforming with carbon dioxide, *Appl. Catal. B: Environ.* 244 (2019) 427–437.

[34] T. Zong, L. Li, Y.J. Han, C.J. Wang, Y. Kang, M. Tian, C.D. Huang, X.D. Wang, Influence of the encapsulation degree of Fe⁰ active sites on performance of garnets for chemical looping partial oxidation of CH₄, *Appl. Catal. B: Environ.* 312 (2022), 121421.

[35] C.S. Wan, K. Song, J.H. Pan, M. Huang, R.Z. Luo, D.L. Li, L.L. Jiang, Ni–Fe/Mg(Al) O alloy catalyst for carbon dioxide reforming of methane: Influence of reduction temperature and Ni–Fe alloying on coking, *Int. J. Hydrog. Energy* 45 (2020) 33574–33585.

[36] J.J. Dai, H.B. Zhang, Evidence of undissociated CO₂ involved in the process of C–H bond activation in dry reforming of CH₄, *J. Catal.* 410 (2022) 266–279.

[37] S. Kim, J. Lauterbach, E. Sasmaz, Yolk–Shell Pt–NiCe@SiO₂ single-atom-alloy catalysts for low-temperature dry reforming of methane, *ACS Catal.* 11 (2021) 8247–8260.

[38] X.L. Yan, W. Sun, L.M. Fan, P.N. Duchesne, W. Wang, C. Kubel, D. Wang, S.G. H. Kumar, Y.F. Li, A. Tavasoli, T.E. Wood, D.L.H. Hung, L.L. Wan, L. Wang, R. Song, J.L. Guo, I. Gourevich, A.A. Jelle, J.J. Lu, R.F. Li, B.D. Hatton, G.A. Ozin, Nickel@Siloxene catalytic nanosheets for high-performance CO₂ methanation, *Nat. Commun.* 10 (2019) 2608.

[39] Q.S. Pan, J.X. Peng, S. Wang, S.D. Wang, In situ FTIR spectroscopic study of the CO₂ methanation mechanism on Ni/Ce_{0.5}Zr_{0.5}O₂, *Catal. Sci. Technol.* 4 (2014) 502–509.

[40] Z.Q. Rao, Y.H. Cao, Z.A. Huang, Z.H. Yin, W.C. Wan, M.Z. Ma, Y.X. Wu, J.B. Wang, G.D. Yang, Y. Cui, Z.M. Gong, Y. Zhou, Insights into the nonthermal effects of light in dry reforming of methane to enhance the H₂/CO ratio near unity over Ni/Ga₂O₃, *ACS Catal.* 11 (2021) 4730–4738.

[41] C. Binet, M. Daturi, J.C. Lavallee, IR study of polycrystalline ceria properties in oxidised and reduced states, *Catal. Today* 50 (1999) 207–225.

[42] A. Westermann, B. Azambre, M.C. Bacariza, I. Graca, M.F. Ribeiro, J.M. Lopes, C. Henriques, The promoting effect of Ce in the CO₂ methanation performances on NiUSY zeolite: A FTIR In Situ/Operando study, *Catal. Today* 283 (2017) 74–81.

[43] L. Azancot, L.F. Bobadilla, M.A. Centeno, J.A. Odriozola, IR spectroscopic insights into the coking-resistance effect of potassium on nickel-based catalyst during dry reforming of methane, *Appl. Catal. B: Environ.* 285 (2021), 119822.

[44] C. Vogt, J. Kranenborg, M. Monai, B.M. Weckhuysen, Structure sensitivity in steam and dry methane reforming over nickel: activity and carbon formation, *ACS Catal.* 10 (2021) 1428–1438.

[45] A. Nandini, K.K. Pant, S.C. Dhingra, K-, CeO₂-, and Mn-promoted Ni/Al₂O₃ catalysts for stable CO₂ reforming of methane, *Appl. Catal. A: Gen.* 290 (2005) 166–174.